


Trace-element composition of pyrite and its implications for hydrothermal process within the Mesoproterozoic metasedimentary sequences of the São Francisco Craton, northeastern Brazil

Elementos traço em pirita e suas implicações para o processo hidrotermal em sequências metassedimentares mesoproterozoicas do Cráton São Francisco, Nordeste do Brasil

Marilane Gonzaga de Melo¹ , Éder Carlos Moreira¹ , Fábio Simplicio¹ , Gláucia Nascimento Queiroga² ,
Letícia Garcia D'Agostim¹ , Marco Paulo de Castro² 

¹Universidade Federal do Espírito Santo - UFES, Departamento de Geologia, Alto Universitário, s/n., CEP 29500-000, Alegre, ES, BR (marilane.melo@ufes.br; eder.c.moreira@ufes.br; fabiogeologo@hotmail.com; leticiadagostim@gmail.com)

²Universidade Federal de Ouro Preto - UFOP, Departamento de Geologia, Laboratório de Microscopia e Microanálises, Ouro Preto, MG, BR (glauuciaqueiroga@ufop.edu.br; marco.castro@ufop.edu.br)

Received on March 11, 2021; accepted on February 9, 2022.

Abstract

The distribution of trace elements in pyrite has been documented for the first time in quartz veins hosted in the Mesoproterozoic metasedimentary sequence of the Tombador Formation, São Francisco Craton, northeast Brazil. In this study, Electron Microprobe Analyses (EPMA) were used to determine the trace-element compositions of pyrite in these hydrothermal quartz veins. Three pyrite types have been distinguished and interpreted from petrographical relationships and trace-element patterns. Pre-existing pyrite (Py₁), derived from the host-rock quartzite, is Ni-poor with concentrations varying from 600 – 6,100 ppm. Elongated syn-tectonic pyrite (Py₂) has similar trace-element composition to the Py₁, with Ni amounts ranging between 830 and 7,870 ppm. In contrast, possibly post-tectonic, euhedral to subhedral hydrothermal pyrite (Py₃), contains higher contents of Ni (7,970 – 26,120 ppm). Mafic and/or metasedimentary rocks from the Espinhaço Supergroup were probably the source of Ni for this fluid-flow event. Fluid generation is related to the devolatilization of the base of the thickened crust, with migration of fluids by preexisting structures. Several shear zones and large-scale NNW-trending folds were developed during the inversion of the Espinhaço basin, as a result of the ca. 0.6 Ga Brasileiro orogenic event. Regional fluid movement through the crust at this time is supported by several mineralized veins and hydrothermal deposits in the São Francisco Craton and adjacent Neoproterozoic belts.

Keywords: Pyrite; Trace elements; Hydrothermal event; Tombador Formation; São Francisco Craton.

Resumo

A distribuição de elementos traço em pirita é documentada pela primeira vez em veios de quartzo hospedados em sequências metassedimentares mesoproterozoicas da Formação Tombador, Cráton São Francisco, Nordeste do Brasil. Neste estudo, análises de microsonda eletrônica (EPMA) foram utilizadas para determinar as composições de elementos traço em pirita nesses veios de quartzo hidrotermal. Três variedades de pirita foram distinguidas e interpretadas com base em relações petrográficas e padrões de elementos traço. A pirita preexistente (Py₁), derivada do quartzito hospedeiro, é pobre em Ni, com concentrações variando de 600 a 6.100 ppm. A pirita alongada sintectônica (Py₂) tem composição de elementos traço similar à de Py₁, com concentrações de Ni entre 830 e 7.870 ppm. Em contraste, a pirita eúdrica a subédrica hidrotermal (Py₃), possivelmente pós-tectônica, contém teores mais elevados de Ni (7.970 – 26.120 ppm). Rochas máficas e/ou metassedimentares do Supergupo Espinhaço foram provavelmente a fonte de Ni para esse evento de fluxo de fluido. A geração de fluidos está relacionada à devolatilização da base da crosta espessada, com migração de fluidos por estruturas preexistentes. Várias zonas de cisalhamento e dobras de tendência NNW em larga escala foram desenvolvidas durante a inversão da bacia Espinhaço, como resultado do evento orogênico Brasileiro de 0,6 Ga. O movimento do fluido regional através da crosta nesse momento é suportado por vários veios mineralizados e depósitos hidrotermais no Cráton São Francisco e cinturões neoproterozoicos adjacentes.

Palavras-chave: Pirita; Elementos traço; Evento hidrotermal; Formação Tombador; Cráton São Francisco.

INTRODUCTION

Sulfide minerals form under a wide variety of conditions in many geological settings. Pyrite is a common iron sulfide in hydrothermal quartz veins and gold deposits (Lindgren, 1933; Agangi et al., 2015; Large and Maslennikov, 2020), as well as in several igneous and metamorphic rocks (Lindgren, 1933; Dias et al., 2019). Pyrite also occurs as detrital grains in sedimentary rocks (Lindgren, 1933; Taylor and Macquaker, 2000; Large et al., 2012; Johnson et al., 2014). Pyrite is stable under various physicochemical fluid conditions and can incorporate appreciable amounts of trace elements at a diverse set of P-T conditions, from diagenesis to high-grade metamorphism (Lindgren, 1933; Roberts, 1982; Agangi et al., 2015). Metamorphic and deformational history can be preserved within single pyrite grains due to their refractory nature (Craig and Vokes, 1993). In addition, trace-element compositions in pyrite can provide important information about its origin. For example, complex zoning patterns within a single pyrite grain can reveal useful information on the solid-state recrystallization and/or dissolution-crystallization processes during metamorphic and/or hydrothermal events (Thomas et al., 2011; Agangi et al., 2015).

In this sense, sulfide-bearing quartz veins hosted in metasedimentary sequences of the northern segment of the São Francisco Craton in northeastern Brazil, have not been investigated for pyrite-stored information. In this study, we investigate the chemical zoning of sulfides within quartz veins hosted in the Mesoproterozoic quartzite that comprises the Tombador Formation in the Espinhaço Supergroup. Microstructural and compositional data indicate different types of pyrite, which are indicative of sedimentary, metamorphic and hydrothermal processes. This study aims to contribute to our understanding of the evolution of hydrothermal fluids and their relationship to the deformational structures generated during the Neoproterozoic Brasiliano event.

GEOLOGICAL SETTING

The São Francisco Craton is a major shield area forming the South American Platform. It is composed of Archean to Paleoproterozoic blocks that were amalgamated during the Rhyacian orogeny, also known as the Transamazonian orogeny (ca. 2.25 – 2.05 Ga) and is surrounded by Neoproterozoic thrust-fold belts resulting from the Brasiliano orogeny (ca. 680 – 500 Ma) (Almeida et al., 1981; Alkmim et al., 1993 — Figure 1A). Cratonic basement rocks comprise Archean to Paleoproterozoic high-grade migmatite and granulite gneisses, as well as granite-greenstone terranes (Teixeira et al., 2000). Paleo-Mesoproterozoic rift-related and associated volcano-plutonic sequences rest on the cratonic basement (Pedreira da Silva, 1994; Guadagnin and Chemale

Jr., 2015; Guadagnin et al., 2015; Guimarães et al., 2005; Magalhães et al., 2015, 2016; Cruz and Alkmim, 2017). In the northern segment of the São Francisco Craton, the supracrustal successions of the Espinhaço Supergroup consist mainly of sandstone, carbonate, volcanic rocks, and mafic dikes, which underwent very low to low-grade metamorphism (Cruz and Alkmim, 2017). In Bahia, these sequences of the Espinhaço Supergroup are divided into two major physiographic domains, the Northern Espinhaço and the Chapada Diamantina, which are separated by the Paramirim valley (Alkmim et al., 1993 — Figure 1B). The study area is located at the Chapada Diamantina Domain, where the supracrustal successions of the Espinhaço Supergroup are split into three groups: Rio dos Remédios, Paraguaçu and Chapada Diamantina (Schobbenhaus and Kaul, 1971; Pedreira da Silva, 1994; Schobbenhaus, 1996; Guimarães et al., 2005) (Figure 2).

The Rio dos Remédios Group comprises a metavolcano-sedimentary sequence, which represents the syn-rift phase of the tectonic evolution of the Espinhaço basin. It includes the continental siliciclastic sequences of the Lagoa de Dentro and Ouricuri do Ouro formations as well as volcanic rocks of the Novo Horizonte Formation (Guimarães et al., 2008). Acid lavas mark the early stage of rifting dated around 1.75 Ga ago (zircon U-Pb age, Babinski et al., 1994, 1999; Schobbenhaus et al., 1994).

The Paraguaçu Group includes the alluvial and eolian deposits of the Mangabeira Formation, which is succeeded by deltaic to shallow marine deposits of the Açuruá Formation (Guimarães et al., 2005; Magalhães et al., 2015). This group is thought to record the post-rift or sag phase of the Espinhaço basin. The upper contact of the Mangabeira Formation with the overlying Açuruá Formation is sharp (Bállico et al., 2017). Mafic sills and dikes cut the lower unit of the Paraguaçu Group and such mafic intrusions are dated at 1514 ± 22 Ma (zircon U-Pb age, Babinski et al., 1999), and 1501 ± 9 Ma (baddeleyite U-Pb age, Silveira et al., 2013).

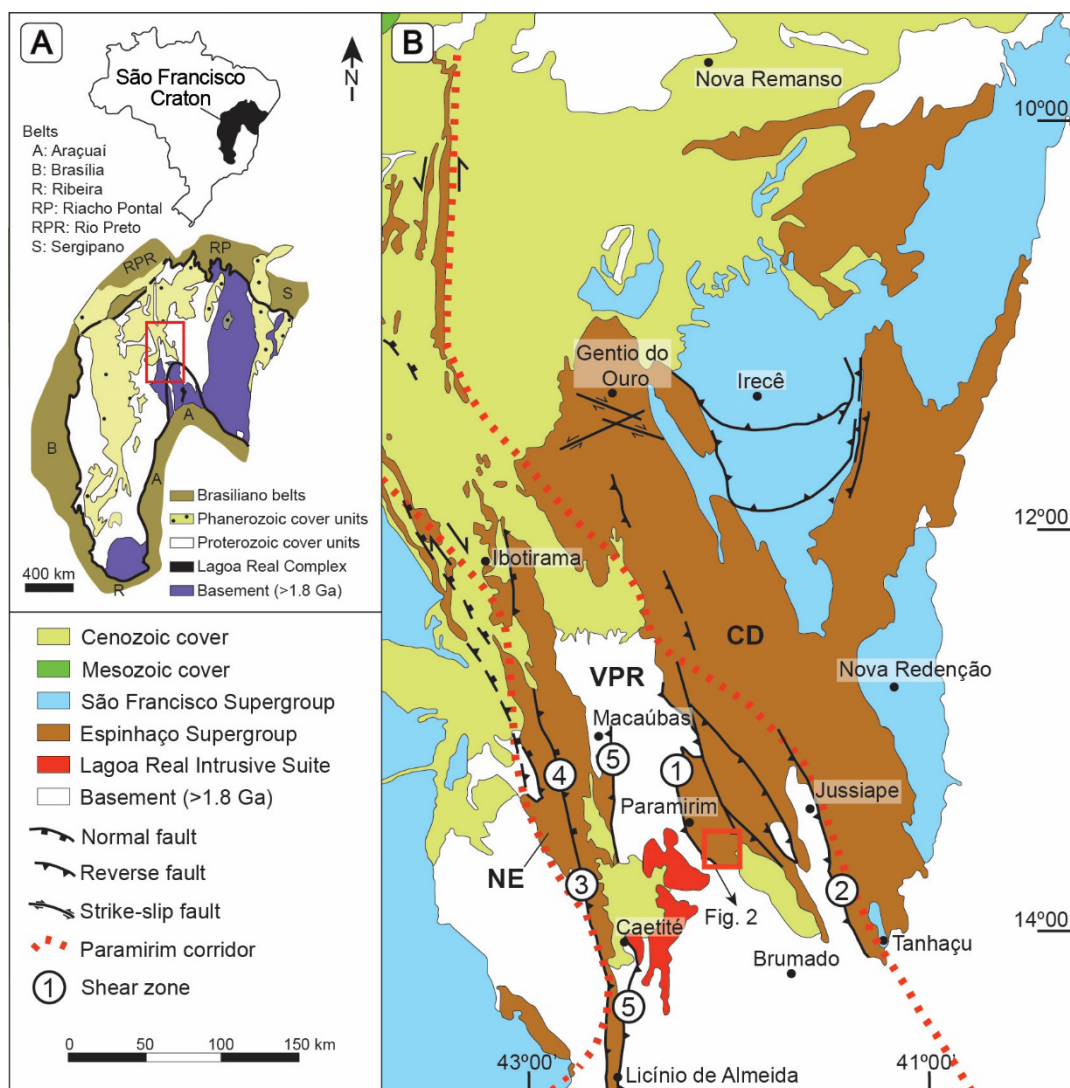
The Chapada Diamantina Group mainly encompasses sandstones and conglomerates formed in continental settings (fluvial, alluvial fan and eolian), as well as estuarine and shallow-marine depositional environments (Guimarães et al., 2008, 2012; Magalhães et al., 2014, 2016). The Tombador Formation, at the base of the group, is composed of braided-fluvial to shallow-marine sandstones and subordinate diamond-bearing conglomerates (Magalhães et al., 2014, 2016). These sandstones are gradually succeeded by the Caboclo Formation, which comprises shallow-marine pelites with subordinate carbonate lenses (Cruz and Alkmim, 2017). The lower contact of the Chapada Diamantina Group is marked by a well-documented angular unconformity over deltaic to shallow-marine deposits of the Açuruá Formation (Pedreira da Silva, 1994; Guimarães et al., 2008; Magalhães

et al., 2015). Crystal-tuff rocks of the upper portion of the Tombador Formation were dated at 1416 ± 28 Ma (zircon U-Pb age, Guadagnin et al., 2015). The youngest detrital zircon population of the Tombador Formation constrains its maximum sedimentation age at ca. 1450 – 1400 Ma (Guadagnin and Chemale Jr., 2015; Guadagnin et al., 2015). Whole-rock Pb-Pb isochrone dating of carbonate rocks in the Caboclo Formation indicates a depositional age of 1140 ± 140 Ma (Babinski et al., 1993).

The Paramirim deformation corridor (Figure 1B), of NNW – SSE orientation, involves the basement rocks and the supracrustal sequences related to the filling of the intracratonic rift (Alkmim et al., 1993). The tectonic fabrics of

the study area define at least three deformation phases (D1, D2 and D3 — Cruz et al., 2007). Evidence for D1 deformation is provided by the nucleation of a thin-skinned system of ESE-verging structures. The D2 deformation phase is characterized by basement-overprinting reverse faults, reverse to oblique-slip ductile shear zones and large-scale NNW-trending folds (Cruz et al., 2007). NNW-oriented and WSW-verging folds associated with crenulation cleavage were developed in high-strain zones during the D3 phase (Cruz et al., 2007).

Textural evidence of hydrothermalism is recorded in some sedimentary sequences from the Chapada Diamantina Group (Cruz et al., 2018). The generation of metamorphic



NE: Northern Espinhaço domain; CD: Chapada Diamantina domain; VPR: Valley of the Paramirim River.

Figure 1. (A) Schematic geological map of the São Francisco Craton and adjacent Brasiliano belts (modified from Alkmim et al., 1993). (B) Simplified geological map of the central-northern segment of the São Francisco Craton, showing the main geological units and tectonic structures of Neoproterozoic age (modified from Cruz, 2004 and Guimarães et al., 2012). Shear zones: 1: Paramirim; 2: Barra do Mendes — João Correia; 3: Santo Onofre; 4: Muquém; and 5: Carrapato.

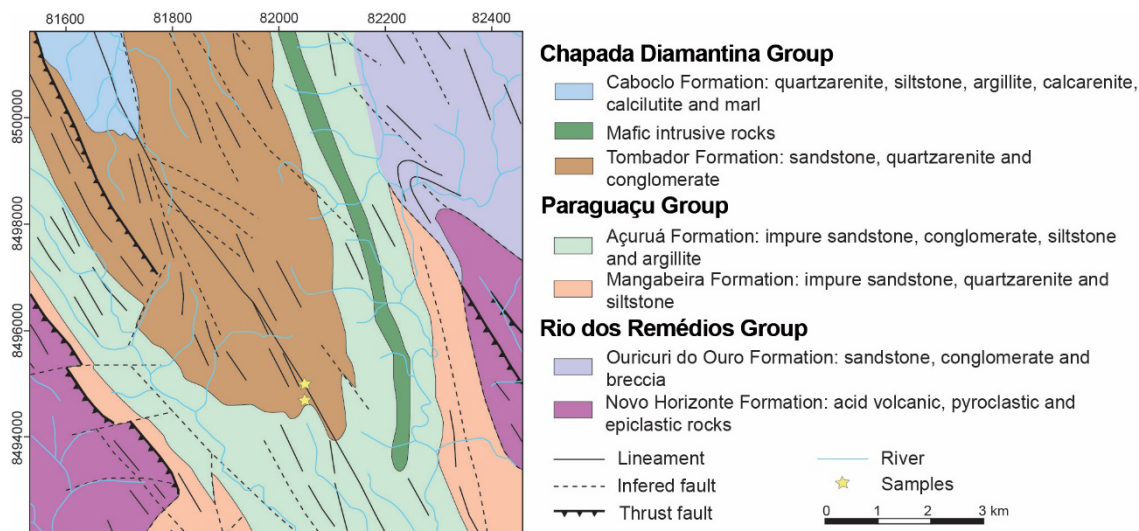


Figure 2. Simplified geological map of the study area (modified from Guimarães et al., 2005), where quartz veins were sampled.

and/or hydrothermal fluids was related to the devolatilization of a thickened crust, with migration of fluids through the preexisting structures (Guimarães et al., 2005, 2012). Gonçalves et al. (2019) have suggested that the fluid generation could have been derived by dehydration of the pelitic sequences in the Espinhaço Supergroup during the Brasiliano event. Regional fluid flow is presented as hydrothermal mineral deposits in the São Francisco Craton and adjacent orogenic belts (e.g., the Araçuai orogen). It includes the Eastern Brazilian Pegmatite Province, Au-Pd deposits, amethyst and baryte hydrothermal deposits (Teixeira et al., 2010; Pedrosa-Soares et al., 2011; Guimarães et al., 2012; Cabral et al., 2015; Cruz et al., 2018). Furthermore, a large number of mineralized veins containing Au, barite-hematite and rutiled quartz are commonly observed in shear zones (Guimarães et al., 2005; Teixeira et al., 2010). Previous geochronological studies have constrained the U-Pb and U-Th-⁴He ages (ca. 524 – 496 Ma) of hydrothermal systems and ore deposits in the São Francisco Craton (e.g., Cabral et al., 2013, 2015). The Paramirim shear zone (see location in Figure 1) was dated at 486 ± 7 Ma using the Ar/Ar method (Guimarães et al., 2005). These ages overlap with U-Pb crystallization ages for hydrothermal minerals (e.g., monazite, xenotime and rutile: ca. 527 – 487 Ma) in the São Francisco Craton and Araçuai belt (Vasconcelos et al., 2018; Gonçalves et al., 2016, 2018, 2019; Santos et al., 2020), attesting to a regional-scale hydrothermal activity at the final stages of the Brasiliano orogenic event.

MATERIALS AND METHODS

The samples for this study were collected from quarries in the Paramirim region, where quartzite rocks of the Tombador

Formation outcrop. Detailed petrography was carried out on quartz-vein samples to identify the mineral phases (sulfides). The mineral abbreviation follows the suggestions of Warr (2021). Pyrite and chalcopyrite grains were analyzed by EPMA (Electron Probe Micro-Analyzer), using a JEOL JXA8230 superprobe, equipped with 5 wavelength-dispersive spectrometers (WDS), at the Laboratory of Microanalysis in the Geology Department, Universidade Federal de Ouro Preto (Brazil). Operating conditions were 20 kV accelerating voltage, 40 nA beam current and 5 μ m beam diameter. Five different spectrometer crystals were used: TAP (in WDS 2); PETH (in WDS 3); LIFH (in WDS 3); LIFL (in WDS 5) and PETL (in WDS 5). The following standards were used for calibration: gold (Au); quartz (Si); Se (Se); indium arsenide (As); gahnite (Zn); silver telluride (Te); indium antimonide (Sb); Co metal (Co); CdS (Cd); silver telluride (Ag); Fe metal (Fe); Bi (Bi); pyrite (S); mercury sulfide (Hg); Cu metal (Cu); Ni metal (Ni); SnO₂ (Sn); Pd metal (Pd); Mn (Mn); Mo metal (Mo); and Pt metal (Pt). Counting time for Au, As, Co and Ni was set to peak at 30 seconds and 15 seconds at the background, while for Si, Se, Zn, Te, Sb, Cd, Ag, Fe, Bi, S, Hg, Cu, Sn, Pd, Mn, Mo and Pt was set to peak at 10 seconds and 5 seconds at background. Major spectral interferences were corrected during the standard and sample measurements. Running conditions and parameters used during EPMA analyses are summarized in Table 1.

RESULTS

Sampling and petrography

The studied area (Figure 2) is economically important for ornamental rocks. There are several quarries in the Paramirim

Table 1. Analytical details of EPMA analyses.

Element	X-ray	Standard	Crystal (Spectrometer)	Peak (s)	Back (s)	Low Bkg (mm)	High Bkg (mm)	LLD (ppm)
Si	K α	Quartz	TAP (2)	15	5	2,739	1,479	170
Fe	K α	Fe	LIFH (3)	15	5	1,204	1,288	290
Ni	K α	Ni	LIFL (5)	30	15	0,714	1,043	250
Cu	K α	Cu	LIFL (5)	15	5	0,665	0,896	280
Zn	L α	Gahnite	TAP (2)	15	5	5,217	2,087	720
Co	K α	Co	LIFH (3)	30	15	1,164	1,304	310
Au	M α	Gold	TAP (2)	30	15	2,050	2,100	1,410
Se	L α	Se	TAP (2)	15	5	5,262	1,955	300
As	L α	Indium arsenide	TAP (2)	30	15	5,566	1,484	860
Te	L α	Silver telluride	PETH (3)	15	5	1,218	1,347	280
Sb	L α	Indium antimonide	PETH (3)	15	5	0,957	1,709	220
Cd	L α	CdS	PETH (3)	15	5	1,565	1,435	235
Ag	L α	Silver telluride	PETH (3)	15	5	1,609	1,174	190
Bi	M α	Bi	PETH (3)	15	5	1,826	1,652	520
S	K α	Pyrite	PETH (3)	15	5	0,739	0,958	345
Hg	M α	Mercury sulfide	PETH (3)	15	5	1,500	1,100	650
Sn	L α	SnO ₂	PETL (5)	15	5	2,348	2,174	230
Pd	L α	Pd	PETL (5)	15	5	1,522	1,261	170
Mn	K α	Mn	LIFL (5)	15	5	1,070	1,117	250
Mo	L α	Mo	PETL (5)	15	5	1,913	1,261	430
Pt	M α	Pt	PETL (5)	15	5	2,695	1,870	400

Bkg: background; LLD: lower limit of detection; SD: standard deviation.

region, some of which are very well exposed in the ridge. In this work, we focused on quartz veins hosted by quartzite rocks of the Tombador Formation (Figure 3). In terms of sedimentological features, the succession consists of quartzite beds ranging between 0.2 and 0.4 m in thickness, with planar and parallel laminae partially interlayered with films of phyllite. Wave ripples and hummocky and swaley cross-beds occur locally. The planar laminae are locally truncated by concave-up structures ranging between 0.2 and 0.4 m in thickness, filled with fine-grained quartzite. The succession of planar laminae is overlapped by clean quartzite with meter-thick sets of trough cross-beds and tangential cross-beds (Figure 3A). The origin of such deposits and sedimentary structures are interpreted as transitional marine to eolian.

Although some sedimentary structures are preserved, shear-zone-related structures (e.g., shear fractures, veins filled by quartz, deformation bands, stylolite, and tension gashes) are commonly observed in the quartzite outcrops (Figures 3A to 3F). At a microscopic scale, a variety of fabrics were formed as a result of strain and recrystallization during shear zone development. It mainly includes S-C fabric and grain-size reduction.

Gray, fine- to medium-grained quartzite rocks are composed of quartz (90 – 97 vol.%), muscovite (2 – 8 vol.%)

and feldspars (1 – 5 vol.%). Zircon, rutile, tourmaline, pyrite and chalcopyrite make up less than 1 vol. %. Quartz occurs both as large porphyroclasts (up to 2 mm across) and as finer grains (< 0.1 mm across) in the rock matrix, with lobate to amoeboid contacts (Figures 4A to 4D). Quartz porphyroclasts present undulose extinction and microstructures that result from dynamic recrystallization by bulging and grain-boundary migration (Figure 4C). Elongated grains are also observed. Some quartz crystals exhibit a polygonal habit with grain triple junction of approximately 120°, typical of static grain growth (Figure 4D). Muscovite occurs as aligned laths between 0.10 and 0.20 mm in length. In a protomylonitic fabric, small muscovite flakes form disconnected trails along the quartz grain boundaries (Figures 4E, 4F). The modal proportion of muscovite increases toward the mylonitic fabric (Figures 4E, 4F). Plagioclase occurs as fine-grained crystals (up to 0.38 mm across). Some K-feldspar grains (0.30 – 0.40 mm across) are fresh and unaltered, whereas others are partially replaced by secondary minerals (e.g., white mica and/or clay minerals). Some K-feldspar porphyroclasts show perthitic intergrowths. Rutile (0.10 – 0.30 mm across) shows well rounded grain shape. Pyrite occurs as anhedral, rounded grains ranging between about 0.2 and 2.0 mm across, in the rock matrix and as elongated, ribbon-like grains within micaceous layers that define the

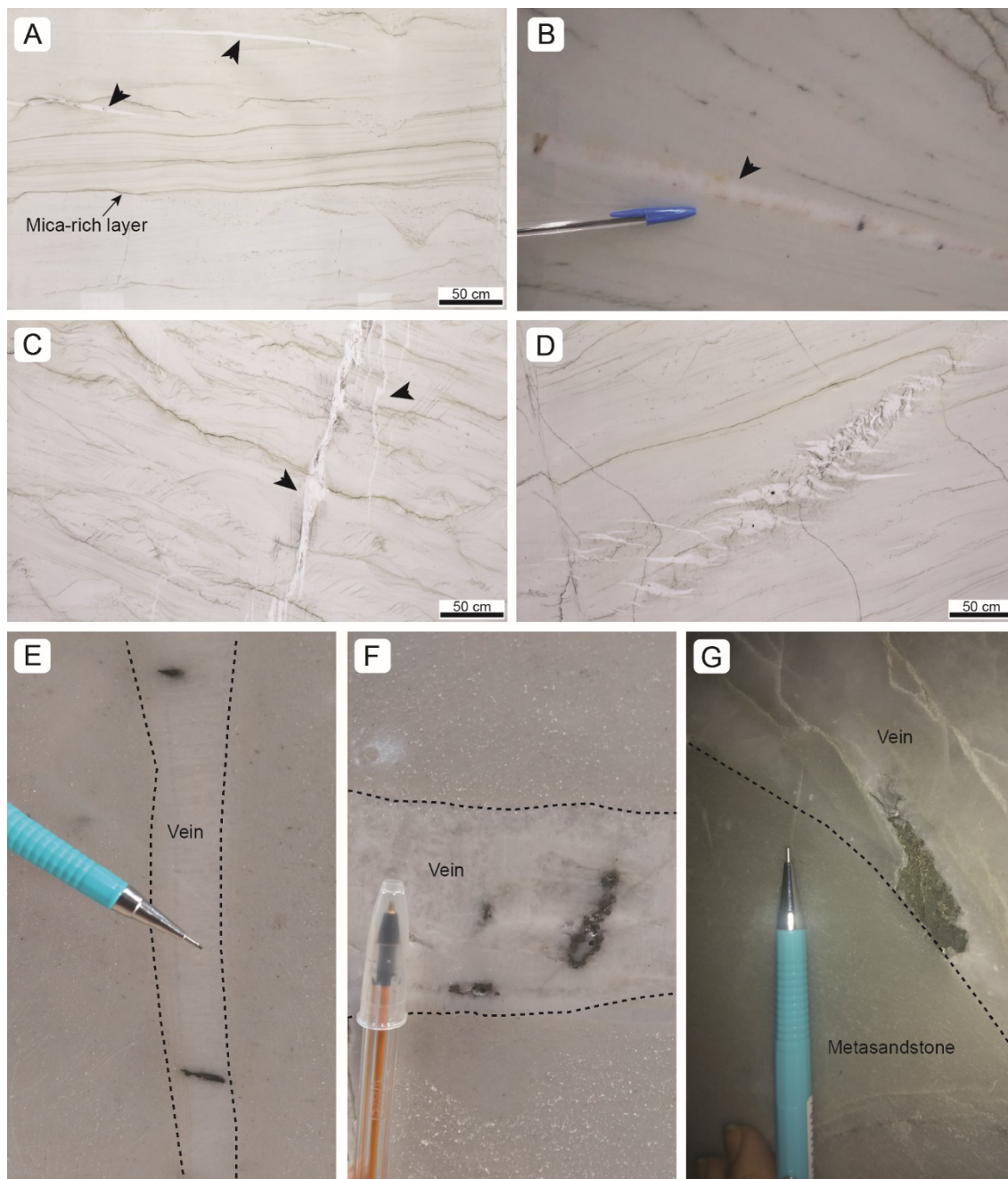


Figure 3. Field photographs and polished slabs showing sedimentary features and quartz veins hosted in quartzite rocks. (A) Quartzite with planar and parallel laminae and concave-up structure with tangential cross-beds (red arrow), and shear structures such as discordant quartz veins (black arrow) and stylolites (dotted lines). (B) Bedding-parallel quartz vein (black arrow). (C) Quartz veins and tension gashes filled by quartz are common. (D, E and F) Veins are dominated by quartz, but locally they present sulfide phases, mostly pyrite.

foliation (Figures 5A, 5B). Chalcopyrite developed along the rim of some anhedral pyrite grains (Figure 5C). Tourmaline (0.06 – 0.20 mm across) is present as rounded, prismatic grains and occasionally as short stumpy rectangular crystals (Figure 5D). Regarding color, the mineral tourmaline

ranges from pale yellow brown to dark brown and blue. Zircon occurs as small, rounded grains between 0.25 and 0.35 mm across.

Quartz veins are found within quartzite rocks, and their dimensions vary in thickness and length, from centimeters to

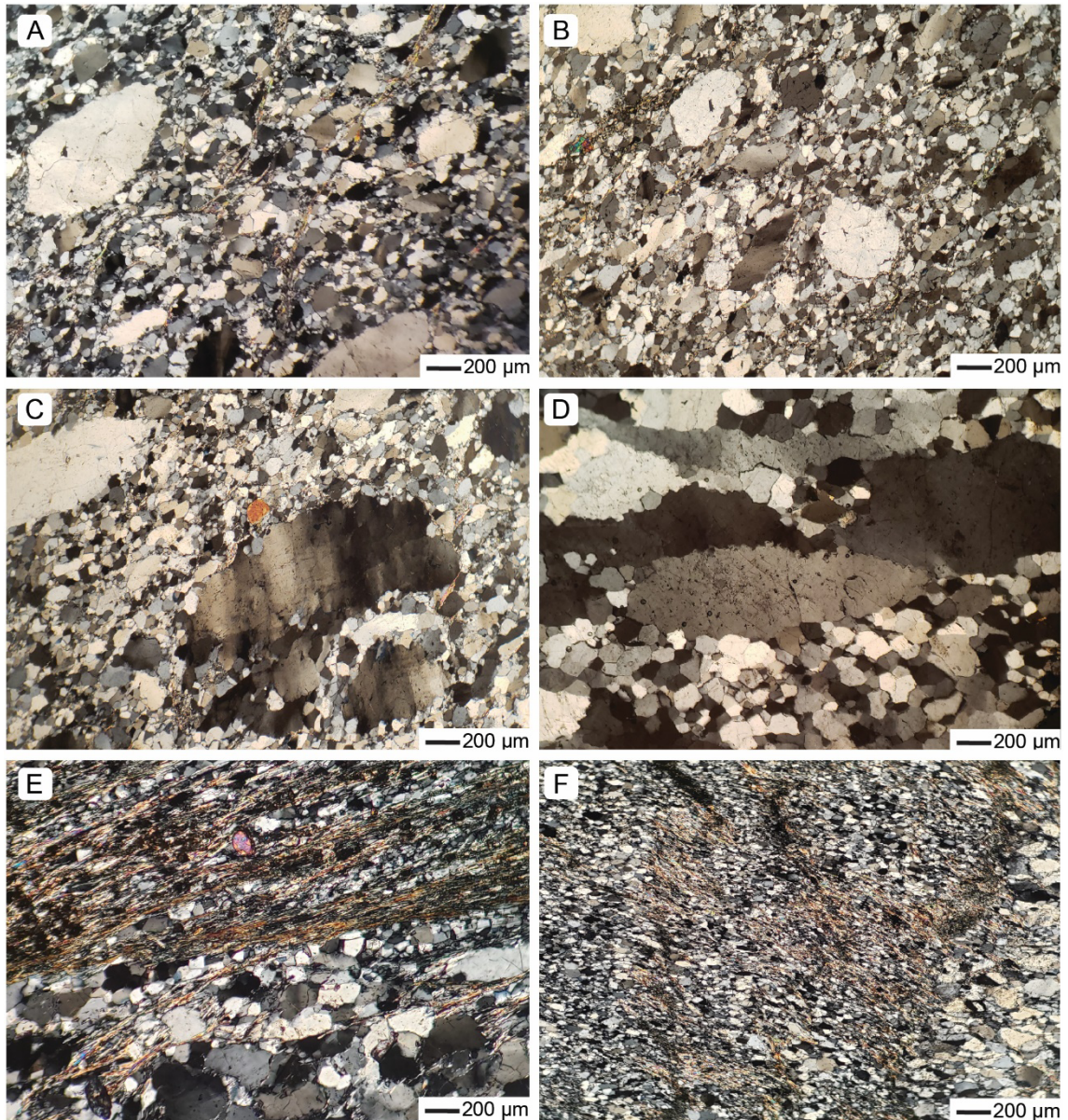


Figure 4. Transmitted-light and crossed-polars photomicrographs of mylonitized quartzite. (A and B) Typical fabric protomylonitic quartzite with abundant quartz porphyroclasts. (C) Quartz with undulose extinction and recrystallization microstructures. (D) Quartz porphyroclasts and small equidimensional grains with contacts at 120° . (E) Mylonite showing a contrast between protomylonitic (lower part) and mylonitic fabric (upper part). (F) Mylonite where the modal proportion of muscovite increases with decreasing quartz grain size.

several meters, respectively (Figure 3). These quartz veins occur at a low angle to the bedding, as well as subperpendicular to it (Figures 3A, 3B). Sigmoidal tension gashes filled by quartz and sulfide form along shear zones (Figure 3C) and both types of veins host sulfide phases (Figures 3D, 3E, 3F). Under the microscope, quartz veins consist of quartz, pyrite, and minor chalcopyrite. Quartz grains are characterized by large anhedral grains (up to 3.75 mm across), forming the main filling of the veins. These grains often exhibit

lobate contacts and undulose extinction (Figures 6A, 6B). At least three types of pyrite are recognized on the basis of distinct microstructures, referred to as Py_1 , Py_2 and Py_3 . The first variety of pyrite (Py_1) occurs as fine-grained rounded or nodular aggregates, which commonly lack abundant inclusions. Some Py_1 grains are surrounded by euhedral to subhedral domains (Py_3) with random silicate inclusions (Figure 6C). The second pyrite type (Py_2) forms ribbon-like laminae that define the foliation-forming pyrite

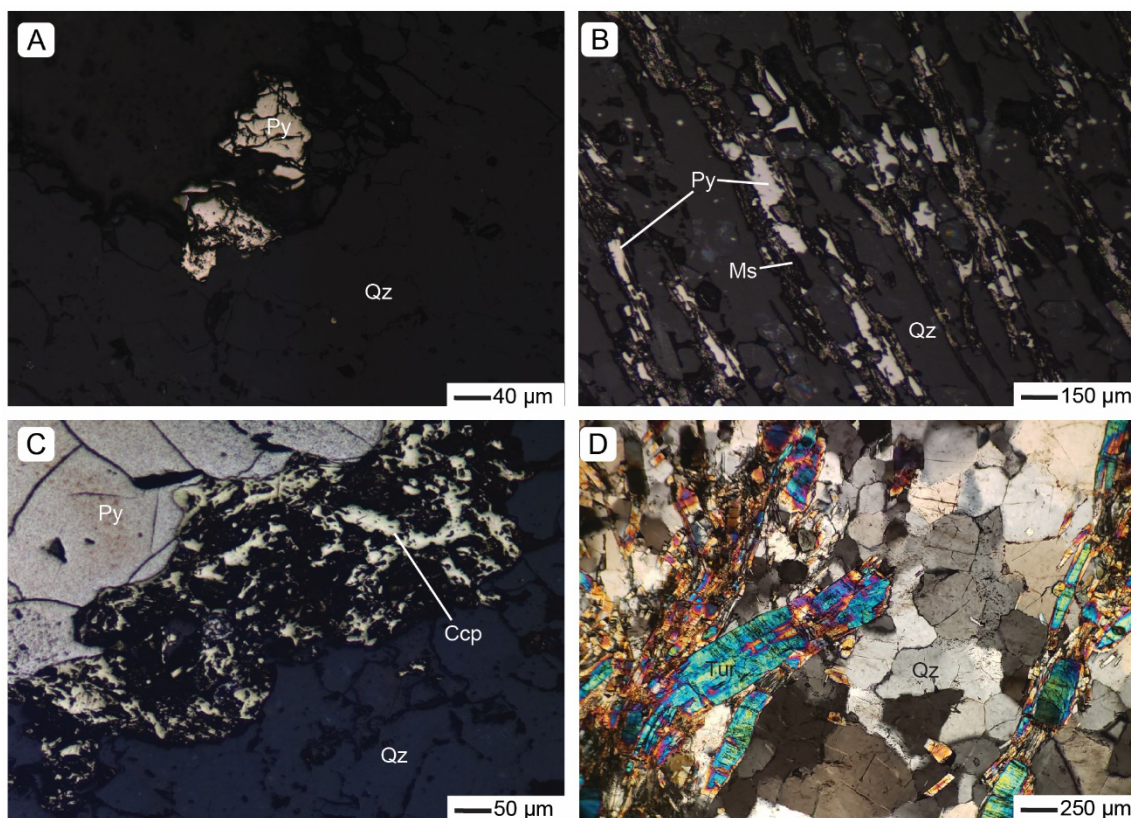


Figure 5. (A to C) Reflected-light and transmitted-light photomicrographs, (D) crossed polars, of quartzite rocks. (A) Anhedral pyrite. (B) Lath-shaped pyrite is aligned along the main foliation, which is defined by the planar arrangement of muscovite. (C) Chalcopyrite along pyrite boundaries. (D) Tourmaline aggregates are oriented along the foliation-forming muscovite.

(Figures 6D, 6E). Chalcopyrite appears to be an overprint on Py_2 (Figures 5B and 6D, 6E). The third pyrite type (Py_3) is presented as sharp, well-defined crystal faces and discrete euhedral to subhedral crystals (Figures 6C, 6F). This variety is the most abundant type observed in the quartz veins of the study area.

Chemical composition of pyrite

EPMA analyses of pyrite and chalcopyrite are reported in Tables 2 to 4. Ni and Cu concentrations for each pyrite type are presented in Figure 7. In addition to the spot analyses, a backscattered-electron composition (BEC) image and quantitative WDS X-ray maps of representative pyrite grains in a quartzite-hosted quartz vein can be found in Figure 8.

Although the trace-element compositions are extremely diverse, Py_1 , Py_2 and Py_3 are distinct from each other. Among all the elements that were measured, Ni is the most abundant, with concentrations ranging from 600 to 26,200 ppm. The Py_1 type presents low Ni contents (600 – 6,100 ppm), locally enriched in Cu (320 – 2,850 ppm)

(Figure 7). As it can be seen in Figure 6, Py_1 is overgrown by inclusion-rich Py_3 domains. The chemical compositions of these Py_3 domains are quite different, being characterized by high contents of Ni in the range of 7,970 to 26,120 ppm (Figure 7). Although ribbon-like Py_2 presents lower Ni (830 – 7,870 ppm) and higher Cu (1450 – 3,440 ppm) contents compared to the Py_3 grains, its chemical composition is similar to that of Py_1 (Figure 7). Chalcopyrite contains relatively high Zn amounts (1,010 – 2,210 ppm).

DISCUSSION

Fabric relationships and trace-element compositions of pyrite can be used to shed light on its origin. In this study, distinct fabric features and trace-element compositions of three pyrite types suggest that they likely have different origins (Figures 6 to 8). We have interpreted the fine-grained rounded pyrite (Py_1) in quartz veins as grains likely derived from the host rock. This interpretation is supported by the presence of disseminated pyrite in quartzite, the fabrics

Figure 6. (A and B) Representative transmitted-light photomicrographs, crossed polars, and (C to F) reflected-light photomicrographs of quartz veins. (A) Contact (red dashed) between the quartz vein and the host quartzite. (B) Large quartz grains (Qz) show evidence of intracrystalline deformation (undulose extinction). (C) Anhedronal pyrite grains (Py₁) surrounded by the inclusion-rich domain (Py₃). (D and E) Ribbon-like pyrite grains (Py₂). Note that chalcopyrite occurs as an overprint on foliation-forming pyrite. (F) Pyrite (Py₃) aggregates mainly occur as subhedronal grains in quartz vein. Note the presence of inclusions in Py₃ (red dashed line).

of which are similar to those shown by the pyrite grains observed in quartz veins (Figure 5A). Pyrite can be transported for long distances before deposition due to its relatively high resistance to mechanical abrasion (hardness of 6.5) (Da Costa et al., 2017). However, the increase in atmospheric oxygen levels in the Paleoproterozoic could result in pyrite oxidation (Da Costa et al., 2017). The occurrence

of pyrite in Mesoproterozoic metasedimentary rocks of the Tombador Formation can be related to physical transport and deposition. In areas with rapid erosion and transport or high aridity, pyrite grains could have been preserved from oxidative weathering (Johnson et al., 2014). The ribbon-like pyrite (Py₂) defines a shear-zone-related foliation with chemical composition similar to the Py₁ grains (Ni-poor

Table 2. Mineral chemistry of pyrite in quartz veins. LLD: lower limit of detection.

Type	Py ₁	Py ₁	Py ₁	Py ₁	Py ₁	Py ₁	Py ₁	Py ₁	Py ₁	Py ₁	Py ₁
Spot	2	4	7	9	15	20	21	22	23	26	31
ppm*											
Si	360	1,410	< LLD	< LLD	300	< LLD	< LLD	170	< LLD	< LLD	< LLD
Fe	472.900	462.480	467.040	476.060	469.400	468.960	467.840	468.170	475.090	464.480	480.590
Ni	2.800	6.100	740	< LLD	2.190	3.710	600	1.280	730	3.870	250
Cu	< LLD	< LLD	< LLD	< LLD	< LLD	< LLD	< LLD	< LLD	< LLD	2,850	< LLD
As	< LLD	< LLD	< LLD	< LLD	< LLD	< LLD	1,180	< LLD	< LLD	< LLD	< LLD
S	520.470	526.950	528.570	519.500	525.260	523.880	519.980	527.910	527.810	526.190	525.180
Type	Py ₁	Py ₁	Py ₁	Py ₁	Py ₁	Py ₁	Py ₁	Py ₁	Py ₁	Py ₁	Py ₂
Spot	32	33	38	39	41	42	43	44	45	46	11
ppm*											
Si	< LLD	< LLD	< LLD	190	< LLD	< LLD	< LLD	< LLD	< LLD	< LLD	< LLD
Fe	465.870	460.620	470.630	463.160	470.830	471.200	473.010	470.020	481.380	478.770	467.970
Ni	< LLD	1.420	1.120	4.150	1.120	1.640	2.790	3.170	720	1.110	3.040
Cu	< LLD	1.840	< LLD	< LLD	320	< LLD	< LLD	350	< LLD	< LLD	1.850
Zn	930	< LLD	< LLD	< LLD	< LLD	< LLD	< LLD	< LLD	< LLD	< LLD	< LLD
S	521.650	522.990	521.770	522.600	518.870	519.690	512.850	519.550	515.620	515.990	523.910

*The following elements were measured for but are below their lower limits of detection: Co, Au, Se, Te, Sb, Cd, Ag, Bi, Hg, Sn, Mo, Pt, Pd and Mn.

Table 3. Mineral chemistry of pyrite in quartz veins. LLD: lower limit of detection.

Type	Py ₂	Py ₂	Py ₂	Py ₂	Py ₃	Py ₃	Py ₃	Py ₃	Py ₃	Py ₃
Spot	27	28	35	37	1	3	5	6	8	10
ppm*										
Si	380	< LLD	< LLD	< LLD	< LLD	< LLD	< LLD	< LLD	< LLD	< LLD
Fe	468.470	478.990	468.140	469.920	460.920	451.140	461.200	455.980	461.300	466.280
Ni	7.870	830	2.490	1.700	12.530	26.160	15.810	19.070	9.520	19.830
Cu	2.380	< LLD	3.440	1.450	< LLD	320	< LLD	< LLD	< LLD	< LLD
Se	< LLD	< LLD	< LLD	< LLD	< LLD	< LLD	< LLD	< LLD	< LLD	340
S	518.520	514.690	519.990	526.120	520.640	522.260	526.500	521.100	518.280	510.530
Type	Py ₃	Py ₃	Py ₃	Py ₃	Py ₃	Py ₃	Py ₃	Py ₃	Py ₃	Py ₃
Spot	14	17	18	19	24	25	29	30	40	47
ppm*										
Si	180	250	< LLD	< LLD	< LLD	< LLD	210	< LLD	< LLD	< LLD
Fe	462.150	465.630	469.020	467.800	469.480	462.520	470.740	461.430	466.610	464.780
Ni	15.150	10.180	15.780	11.000	7.970	16.540	9.240	17.980	12.550	14.470
Zn	< LLD	< LLD	< LLD	< LLD	< LLD	< LLD	1.260	< LLD	< LLD	< LLD
Te	< LLD	< LLD	< LLD	310	< LLD	< LLD	< LLD	< LLD	< LLD	< LLD
S	518.790	518.470	514.470	517.000	518.850	519.590	512.890	517.960	511.450	510.780

*The following elements were measured for but are below their lower limits of detection: Co, Au, Sb, Cd, Ag, Bi, Hg, Sn, Mo, Pt, Pd and Mn.

grains). Grain elongation likely occurred during progressive ductile deformation. The Ni-rich euhedral to subhedral pyrite grains (Py₃), as well as Ni-rich overgrowths on Py₁, are interpreted to be of hydrothermal origin (Figures 6 to 8), likely having been formed late or after the deformation event that affected the early grains.

Py₁ and Py₂ have a distinct trace-element composition compared to Py₃ (Figure 7). In contrast, both Py₁ and Py₂ show similar trace-element compositions. These data suggest that the distinct domains of pyrite grains were formed at different stages and under different physicochemical conditions. Incorporation of trace elements into pyrite can occur either via invisible solid solution within the pyrite structure or as inclusions of nanoscale particles (Large et al., 2009;

Table 4. Mineral chemistry of chalcopyrite in quartz veins.

Type	Ccp	Ccp	Ccp	Ccp	Ccp
Spot	13	34	36	48	49
ppm*					
Si	200	530	700	1.040	1.540
Fe	306.460	310.740	310.130	313.080	300.740
Ni	420	310	< LLD	< LLD	< LLD
Cu	338.730	342.400	335.080	333.450	325.880
Zn	1.010	< LLD	< LLD	< LLD	2.210
Se	< LLD	350	< LLD	< LLD	< LLD
S	344.240	341.220	349.660	344.570	308.200
Pt	< LLD	< LLD	< LLD	480	< LLD

*The following elements were measured for but are below their lower limits of detection: Co, Au, As, Te, Sb, Cd, Ag, Bi, Hg, Sn, Mo, Pd and Mn; LLD: lower limit of detection.

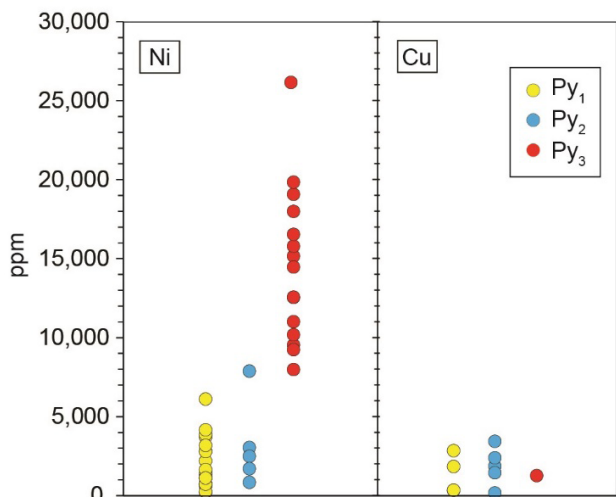


Figure 7. Diagram showing the concentration of Ni and Cu in different types of pyrite in quartz veins. Note that the Py_3 grains are the most enriched in Ni.

Thomas et al., 2011; Agangi et al., 2015). As it can be seen in Figure 8, pyrite in quartz veins shows a prominent zoning of Ni, indicated by Ni-poor pyrite growth zones truncated by domains of pyrite with high Ni contents. The abundance of Ni varies inversely with Fe and there is no clear trend with S, suggesting that Ni occupies the Fe site rather than the S site in the pyrite structure (Figures 9A, 9B). Cu contents show no clear relation with Fe and S (Figures 9C, 9D). Based on chemical relationships, Ni is considered to enter the pyrite structure and Cu could occur as Cu-sulfide nanoinclusions. The presence of chalcopyrite spatially associated with Py_1 , as well as overprint on Py_2 (Figures 5C and 6D, 6E), can contribute to the high values of Cu observed in some pyrite grains.

The high contents of Ni in hydrothermal pyrite can indicate:

- Ni leaching from wall rocks and/or metasedimentary package and its subsequent redistribution;
- the influence of a mafic source.

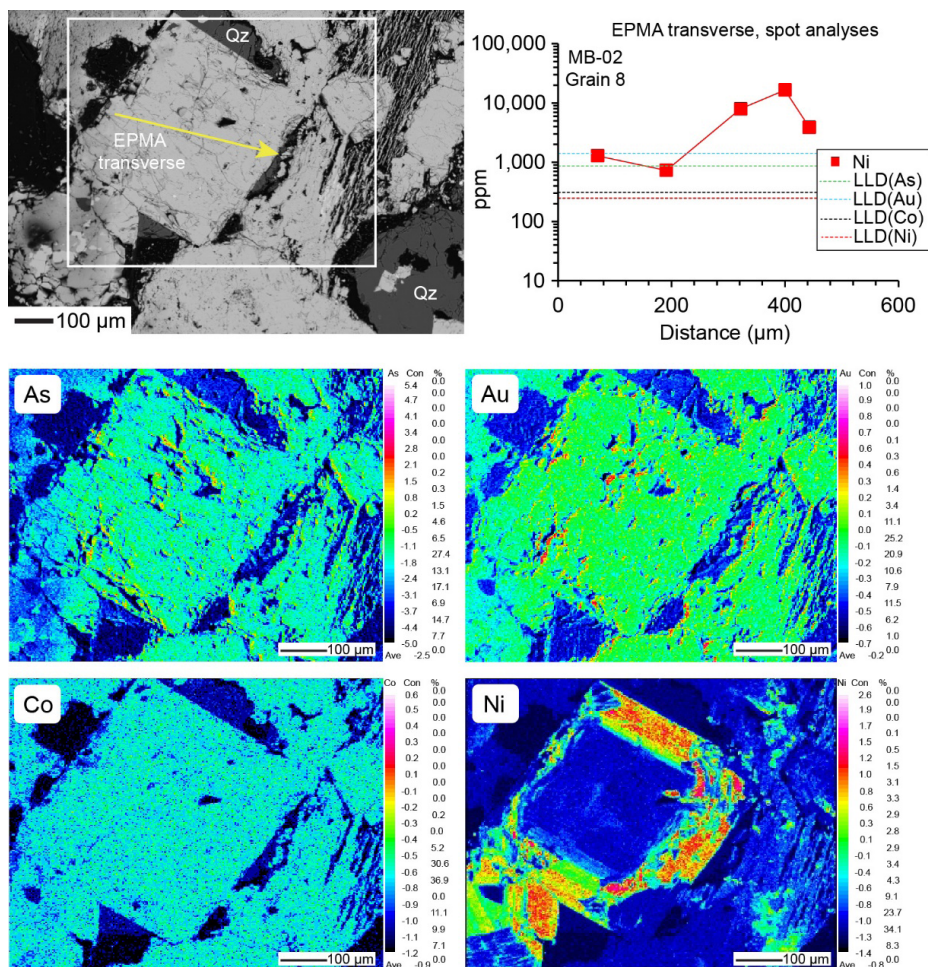


Figure 8. Backscattered-electron composition (BEC) and electron probe micro-analyzer (EPMA) images of pyrite grains (sample MB-02). Note different amounts of Ni between core (Py_1) and rim (Py_3) domains. As, Au and Co contents are below the lower limit of detection (LLD).

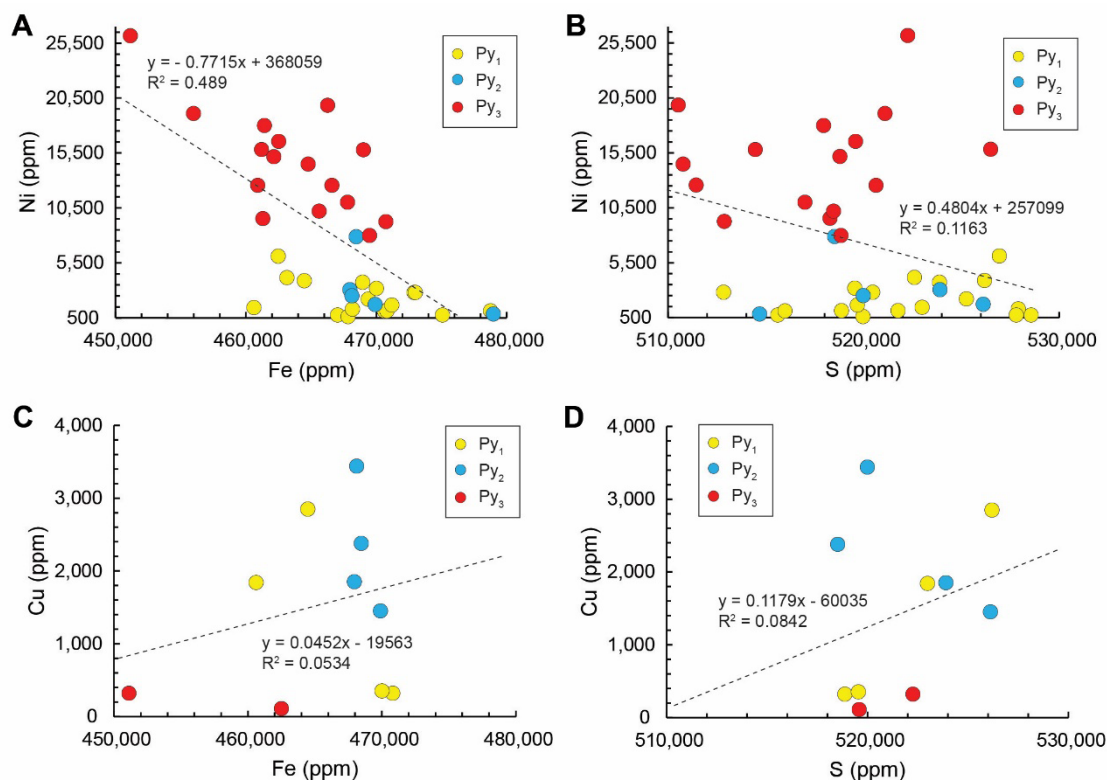


Figure 9. Scattergrams of some element concentrations in pyrite. (A) Ni vs. Fe, (B) Ni vs. S, (C) Cu vs. Fe and (D) Cu vs. S.

The host quartzite likely did not release Ni amounts to the hydrothermal fluid since alteration halos around the quartz veins were not observed (Figure 3). The supracrustal sequence (clastic sedimentary) of the São Francisco Craton is predominantly composed of quartzite/sandstone, with subordinate levels of metaconglomerate, metargillite, metasiltite and metarhytmite. Cr and Ni are preferentially incorporated in argillaceous rather than in sandy sediments. Field relationships show thin alteration layers adjacent to the quartz veins hosted in pelitic sequences from the Chapada Diamantina Group (e.g., Cruz et al., 2018). Ni amounts could be leached from these pelitic levels. Mafic dykes (~1.5 Ga) are embedded in the Archean basement rocks, as well as metasedimentary rocks of the Espinhaço Supergroup (Brito, 2008; Varjão and Leal, 2019). As it can be observed in Figure 2, mafic intrusions occur close to the studied quarries. According to previous geochemical studies (Brito, 2008; Teixeira, 2008; Varjão and Leal, 2019), the mafic dikes and sills in the study area show a relatively high Ni concentration (up to 253 ppm), and can be considered the Ni source for the hydrothermal fluid. These dykes present evidence of hydrothermal alteration, which has resulted in secondary mineral phases (Varjão and Leal, 2019). These spatial relationships combined with the trace-element composition

of pyrite, suggest that the quartz veins acted as channels for hydrothermal fluid flow carrying Ni from the mafic rocks and/or sedimentary sequences in the study area.

Deformational structures (e.g., shear zones and fault) are important channels for the fluid movement through the crust (Cox, 2002; Mancktelow, 2006; Ague, 2014). Fluid migration through shear zones and/or regional faults may affect the shear strength of these structures, promoting chemical reactions between the fluid and the rock, as well as inducing changes in fluid pressure (Cox, 2002; Ague, 2014). The quartzite sequence of the Tombador Formation records evidence of deformation, low-grade metamorphism, and hydrothermal activity (Figures 2 and 3). Several NNW–SSE trending shear zones were developed during the inversion of the Espinhaço basin (see some of them in Figure 1), and such structures could have been important conducts of hydrothermal fluids (Alkmim et al., 1993; Cruz and Alkmim, 2017). In addition, sedimentary structures could have favored the flow of the hydrothermal fluid from shear zones along the supracrustal sequences of the Espinhaço Supergroup (Teixeira et al., 2010; Cruz et al., 2018). In the study area, numerous quartz veins cut quartzite rocks and display strong structural control (Figures 3A to 3C). Bedding-parallel veins and discordant veins are probably contemporaneous, related to the regional-scale fold-and-thrust

tectonics. Field features show that bedding-parallel fluid flow took place along pre-existing fractures and/or close to the mica-rich layers (Figure 3A). Such structures are commonly interpreted as sources of permeability anisotropy (e.g., Ague, 2014). The presence of tension gashes filled with quartz and sulfide (Figure 3C) speaks in favor of an extensional fracture associated with shear-zone development.

CONCLUSION

There are several structurally controlled sulfide-bearing quartz veins hosted by metasedimentary rocks of the Tombador Formation (Espinhaço Supergroup). Our data show that different generations of pyrite (Py₁, Py₂ and Py₃) have characteristic trace-element patterns, which can be used as a tracer for sedimentary, metamorphic and hydrothermal processes. The earliest pyrite type (Py₁) is poor in Ni and may have derived from the host rock, whereas Ni-poor elongated pyrite (Py₂) was formed during ductile deformation. Subsequently, the Ni-rich pyrite of hydrothermal origin (Py₃) occurred late or after the deformation event. The geological conditions for the development of quartz veins were created during the Brasiliano orogenic event. The generation of metamorphic-hydrothermal fluids was related to the devolatilization reactions, promoted in response to crustal thickening. In study area, the high-Ni contents observed in Py₃ grains were likely derived from leaching of the metamafic rocks and/or pelitic sequences during the hydrothermal event.

ACKNOWLEDGEMENTS

This work is part of the Project n° 10044/2019 registered in PRPPG (UFES). The authors acknowledge the financial and field support provided by Decolores Mármore e Granitos do Brasil Ltda. We thank to the Microscopy and Microanalysis Laboratory (LMic) of UFOP, a member of FAPEMIG supported Microscopy and Microanalysis Network of Minas Gerais. G. Queiroga is fellow of the Brazilian Research Council (CNPq) and acknowledge the received support. We thank Alexandre Raphael Cabral and one anonymous reviewer for their constructive and helpful suggestions which greatly improved our manuscript.

REFERENCES

- Agangi, A., Przybyłowicz, W., Hofmann, A. (2015). Trace element mapping of pyrite from Archean gold deposits – A comparison between PIXE and EPMA. *Nuclear Instruments and Methods in Physics Research Section B: Beam Interactions with Materials and Atoms*, 348, 302-306. <https://doi.org/10.1016/j.nimb.2014.11.070>
- Ague, J. J. (2014). Fluid flow in the deep crust. In: H. D. Holland, K. K. Turekian (Eds.). *Treatise on Geochemistry*, v. 4, p. 203-247. 2. ed. Los Angeles: Elsevier. <https://doi.org/10.1016/B978-0-08-095975-7.00306-5>
- Alkmim, F. F., Brito Neves, B. B., Alves, J. A. C. (1993). Arcabouço tectônico do Cráton do São Francisco – uma revisão. In: J. M. Dominguez, A. Misi (Eds.). *O cráton do São Francisco*, p. 45-62. Salvador: SBG/Núcleo BA/SE/SGM/CNPq.
- Almeida, F. F. M., Hasui, Y., Brito Neves, B. B., Fuck, R. A. (1981). Brazilian structural provinces: an introduction. *Earth and Science Reviews*, 17(1-2), 1-29. [https://doi.org/10.1016/0012-8252\(81\)90003-9](https://doi.org/10.1016/0012-8252(81)90003-9)
- Babinski, M., Brito-Neves, B. B., Machado, N., Noce, C. M., Ulhein, A., Van Schmus, W. R. (1994). Problemas na metodologia U/Pb em zircões de vulcânicas continentais: o caso do Grupo Rio dos Remédios, Supergroup Espinhaço, no estado da Bahia. *XXXVIII Congresso Brasileiro de Geologia*, 409-410. Camboriú: Brazilian Geological Society.
- Babinski, M., Pedreira, A. J., Brito Neves, B. B., Van Schmus, W. R. (1999). Contribuição à geocronologia da Chapada Diamantina. *VII Simpósio Nacional de Estudos Tectônicos*, 118-120. Recife: Brazilian Geological Society.
- Babinski, M., Van Schmus, W. R., Chemale Jr., F., Brito Neves, B. B., Rocha, A. J. D. (1993). Idade isocrônica Pb/Pb em rochas carbonáticas da Formação Caboclo em Morro do Chapéu. *II Simpósio sobre o Craton do São Francisco*, 160-163. Salvador: Brazilian Geological Society.
- Bállico, M. B., Scherer, C. M. S., Mountney, N. P., Souza, E. G., Reis, A. D., Raja Gabaglia, G. P., Magalhães, A. J. C. (2017). Sedimentary cycles in a Mesoproterozoic aeolian erg-margin succession: Mangabeira Formation, Espinhaço Supergroup, Brazil. *Sedimentary Geology*, 349, 1-14. <https://doi.org/10.1016/j.sedgeo.2016.12.008>
- Brito, D. C. (2008). *Geologia, petrografia e litogeoquímica dos diques máficos que ocorrem na porção sudoeste da Chapada Diamantina, Bahia, Brasil*. Dissertation (Master). Bahia: Instituto de Geociências - UFBA.
- Cabral, A. R., Eugster, O., Brauns, M., Lehmann, B., Rösel, D., Zack, T., Abreu, F. R., Pernicka, E., Barth, M. (2013). Direct dating of gold by radiogenic helium: testing the method on gold from Diamantina, Minas Gerais, Brazil. *Geology*, 41(2), 163-166. <https://doi.org/10.1130/G33751.1>

- Cabral, A. R., Zeh, A., Galbiatti, H. F., Lehmann, B. (2015). Late Cambrian Au-Pd mineralization and Fe enrichment in the Itabira district, Minas Gerais, Brasil, at 496 Ma: constraints from U-Pb monazite dating of a Jacutinga lode. *Economic Geology*, 110(1), 263-272. <https://doi.org/10.2113/econgeo.110.1.263>
- Cox, S. F. (2002). Fluid flow in mid- to deep crustal shear systems: Experimental constraints, observations on exhumed high fluid flux shear systems, and implications for seismogenic processes. *Earth Planets Space*, 54, 1121-1125. <https://doi.org/10.1186/BF03353312>
- Craig, J. R., Vokes, F. M. (1993). The metamorphism of pyrite and pyritic ores-an overview. *Mineralogical Magazine*, 57(386), 3-18. <https://doi.org/10.1180/minmag.1993.057.386.02>
- Cruz, S. C. P. (2004). *A interação tectônica entre o aulacógeno do Paramirim e o orógeno Araçuai-Oeste Congo*. Thesis (Doctorate). Ouro Preto: Departamento de Geologia - UFOP.
- Cruz, S. C. P., Alkmim, F. F. (2017). The Paramirim Aulacogen. In: M. Heilbron, U. G. Cordani, F. F. Alkmim (Eds.), *São Francisco Craton, Eastern Brazil*, v. 1, p. 97-115. Cham: Springer. <https://doi.org/10.1007/978-3-319-01715-0>
- Cruz, S. C. P., Dias, V. M., Alkmim, F. F. (2007). A interação tectônica embasamento/coertura em aulacógenos invertidos: um exemplo da Chapada Diamantina Ocidental. *Revista Brasileira de Geociências*, 37(4), 111-127. <https://doi.org/10.25249/0375-7536.200737S411127>
- Cruz, V. A., Cruz, S. C. P., Lobato, L. M., Rios, F. J., Santos, J. S., Lima, G. M. P. (2018). Structural control and hydrothermal evolution model of unusual, high-grade metasandstone-hosted iron deposits, Mesoproterozoic eastern Chapada Diamantina, Brazil. *Ore Geology Reviews*, 101, 221-272. <https://doi.org/10.1016/j.oregeorev.2018.06.003>
- Da Costa, G., Hofmann, A., Agangi, A. (2017). Provenance of detrital pyrite in Archean sedimentary rocks: examples from the Witwatersrand Basin. In: R. Mazumder (Ed.), *Sediment provenance: influences on compositional change from source to sink*, v. 1, p. 509-531. Amsterdam: Elsevier. <https://doi.org/10.1016/B978-0-12-803386-9.00018-6>
- Dias, J. C. S., Gonçalves, L., Gonçalves, C. C. (2019). Contrasting oxygen fugacity of I- and S-type granites from the Araçuai orogen, SE Brazil: an approach based on opaque mineral assemblages. *Mineralogy and Petrology*, 113, 667-686. <https://doi.org/10.1007/s00710-019-00670-2>
- Gonçalves, G. O., Lana, C., Buick, I. S., Alkmim, F. F., Scholz, R., Queiroga, G. (2019). Twenty million years of post-orogenic fluid production and hydrothermal mineralization across the external Araçuai orogen and adjacent São Francisco craton, SE Brazil. *Lithos*, 342-343, 557-572. <https://doi.org/10.1016/j.lithos.2019.04.022>
- Gonçalves, G. O., Lana, C., Scholz, R., Buick, I. S., Gerdes, A., Kamo, S. L., Corfu, F., Marinho, M. M., Chaves, A. O., Valeriano, C., Nalini Jr., H. A. (2016). An assessment of monazite from the Itambé pegmatite district for use as U-Pb isotope reference material for microanalysis and implications for the origin of the “Moacyr” monazite. *Chemical Geology*, 424, 30-50. <https://doi.org/10.1016/j.chemgeo.2015.12.019>
- Gonçalves, G. O., Lana, C., Scholz, R., Buick, I. S., Gerdes, A., Kamo, S. L., Corfu, F., Rubatto, D., Wiedenbeck, M., Nalini Jr., H. A., Oliveira, L. C. (2018). The diamantina monazite: a new low-Th reference material for microanalysis. *Geostandards and Geoanalytical Research*, 42(1), 25-47. <https://doi.org/10.1111/ggr.12192>
- Guadagnin, F., Chemale Jr., F. (2015). Detrital zircon record of the Paleoproterozoic to Mesoproterozoic cratonic basins in the São Francisco Craton. *Journal of South American Earth Sciences*, 60, 104-116. <https://doi.org/10.1016/j.jsames.2015.02.007>
- Guadagnin, F., Chemale Jr., F., Magalhães, A. J. C., Santana, A., Dussin, I., Takehara, L. (2015). Age constraints on crystal-tuff from the Espinhaço Supergroup – Insight into the Paleoproterozoic to Mesoproterozoic intracratonic basin cycles of the Congo-São Francisco Craton. *Gondwana Research*, 27(1), 363-376. <https://doi.org/10.1016/j.gr.2013.10.009>
- Guimarães, J. T., Alkmim, F. F., Cruz, S. C. P. (2012). Supergrupos Espinhaço e São Francisco. In: J. S. F. Barbosa, J. F. Mascarenhas, L. C. C. Gomes, J. M. L. Dominguez, J. S. Souza (Eds.). *Geologia da Bahia: pesquisa e atualização*, v. 13, p. 33-85. Salvador: CBPM.
- Guimarães, J. T., Martins, A. M., Andrade Filho, E. L., Loureiro, H. C., Arcanjo, J. B., Neves, J. P., Abram, M. B., Silva, M. G., Melo, R. C., Bento, R. V. (2005). *Projeto Ibitiara-Rio de Contas: estado da Bahia. Escala 1:200.000*. Salvador: Programa Recursos Minerais do Brasil/CPRM.
- Guimarães, J. T., Santos, R. A., Melo, R. C. (2008). *Geologia da Chapada Diamantina Ocidental (Projeto Ibitiara-Rio de Contas)*. Salvador: Companhia Baiana de Pesquisa Mineral – CBPM/Companhia Pesquisa de Recursos Minerais – CPRM. Série Arquivos Abertos, 31, 64.

- Johnson, J. E., Gerpheide, A., Lamb, M. P., Fischer, W. W. (2014). O₂ constraints from Paleoproterozoic detrital pyrite and uraninite. *Geological Society of America Bulletin*, 126(5-6), 813-830. <https://doi.org/10.1130/B30949.1>
- Large, R. R., Danyushevsky, L., Hollit, C., Maslennikov, V., Meffre, S., Gilbert, S., Bull, S., Scott, R., Emsbo, P., Thomas, H., Singh, B., Foster, J. (2009). Gold and trace element zonation in pyrite using a laser imaging technique: implications for the timing of gold in Orogenic and Carlin-style sediment-hosted deposits. *Economic Geology*, 104(5), 635-668. <https://doi.org/10.2113/gsecongeo.104.5.635>
- Large, R. R., Maslennikov, V. V. (2020). Invisible gold paragenesis and geochemistry in pyrite from orogenic and sediment-hosted gold deposits. *Minerals*, 10(4), 339. <https://doi.org/10.3390/min10040339>
- Large, R. R., Thomas, T., Craw, D., Henne, A., Henderson, S. (2012). Detrital pyrite as a source for metals in orogenic gold deposits, Otago Schist, New Zealand. *New Zealand Journal of Geology and Geophysics*, 55(2), 137-149. <https://doi.org/10.1080/00288306.2012.682282>
- Lindgren, W. (1933). *Mineral Deposits*. New York: McGraw-Hill.
- Magalhães, A. J. C., Raja Gabaglia, G. P., Scherer, C. M. S., Bállico, M. B., Guadagnin, F., Bento Freire, E., Silva Born, L. R., Catuneanu, O. (2016). Sequence hierarchy in a Mesoproterozoic interior sag basin: from basin fill to reservoir scale, the Tombador Formation, Chapada Diamantina Basin, Brazil. *Basin Research*, 28(3), 393-432. <https://doi.org/10.1111/bre.12117>
- Magalhães, A. J. C., Scherer, C. M. S., Raja Gabaglia, G. P., Bállico, M. B., Catuneanu, O. (2014). Unincised fluvial and tide-dominated estuarine systems from the Mesoproterozoic Lower Tombador Formation, Chapada Diamantina basin, Brazil. *Journal South American Earth Science*, 56, 68-90. <https://doi.org/10.1016/j.jsames.2014.07.010>
- Magalhães, A. J. C., Scherer, C. M. S., Raja Gabaglia, G. P., Catuneanu O. (2015). Mesoproterozoic delta systems of the Açuruá Formation, Chapada Diamantina, Brazil. *Precambrian Research*, 257, 1-21. <https://doi.org/10.1016/j.precamres.2014.11.016>
- Mancktelow, N. S. (2006). How ductile are ductile shear zones? *Geology*, 34(5), 345-348. <https://doi.org/10.1130/G22260.1>
- Pedreira da Silva, A. J. C. L. (1994). *O Supergrupo Espinhaço na Chapada Diamantina Centro-Oriental, Bahia: sedimentação, estratigrafia e tectônica*. Thesis (Doctorate). São Paulo: Instituto de Geociências - USP. <https://doi.org/10.11606/T.44.1994.tde-10112015-155542>
- Pedrosa-Soares, A. C., Campos, C. P., Noce, C., Silva, L. C., Novo, T., Roncato, J., Medeiros, S., Castañeda, C., Queiroga, G., Dantas, E., Dussin, I., Alkmim, F. (2011). Late Neoproterozoic–Cambrian granitic magmatism in the Araçuaí orogen (Brazil), the Eastern Brazilian Pegmatite Province and related mineral resources. *Geological Society of London, Special Publications*, 350, 25-51. <https://doi.org/10.1144/SP350.3>
- Roberts, F. I. (1982). Trace element chemistry of pyrite: A useful guide to the occurrence of sulfide base metal mineralization. *Journal of Geochemical Exploration*, 17(1), 49-62. [https://doi.org/10.1016/0375-6742\(82\)90019-X](https://doi.org/10.1016/0375-6742(82)90019-X)
- Santos, M. M., Lana, C., Scholz, R., Buick, I. S., Kamo, S. L., Corfu, F., Queiroga, G. (2020). LA-ICP-MS U-Pb dating of rutiles associated with hydrothermal mineralization along the southern Araçuaí Belt, SE Brazil. *Journal of South American Earth Sciences*, 99, 102502. <https://doi.org/10.1016/j.jsames.2020.102502>
- Schobbenhaus, C. (1996). As tafrogêneses superpostas Espinhaço e Santo Onofre, Estado da Bahia: revisão e novas propostas. *Revista Brasileira de Geociências*, 26(4), 265-276. <https://doi.org/10.25249/0375-7536.19964265276>
- Schobbenhaus, C., Kaul, P. T. (1971). Contribuição à estratigrafia da Chapada Diamantina Bahia-Central. *Mineração e Metalurgia*, 53(315), 116-120.
- Schobbenhaus, C., Hoppe, A., Baumann, A., Lork, A. (1994). Idade U/Pb do vulcanismo Rio dos Remédios, Chapada Diamantina, Bahia. *XXXVIII Congresso Brasileiro de Geologia*, 2, 397-398. Camboriú: SBG.
- Silveira, E. M., Söderlund, U., Oliveira, E. P., Ernst, R. E., Leal, A. B. M. (2013). First precise U–Pb baddeleyite ages of 1500 Ma mafic dykes from the São Francisco Craton, Brazil, and tectonic implications. *Lithos*, 174, 144-156. <https://doi.org/10.1016/j.lithos.2012.06.004>
- Taylor, K. G., Macquaker, J. H. S. (2000). Early detrital pyrite morphology in a mudstone-dominated succession: the Lower Jurassic Cleveland Ironstone Formation, eastern England. *Sedimentary Geology*, 131(1-2), 77-86. [https://doi.org/10.1016/S0037-0738\(00\)00002-6](https://doi.org/10.1016/S0037-0738(00)00002-6)

- Teixeira, J. B. G., Silva, M. G., Misi, A., Cruz, S. C. P., Sá, J. H. S. (2010). Geotectonic setting and metallogeny of the northern São Francisco craton, Bahia, Brazil. *Journal of South American Earth Sciences*, 30(2), 71-83. <https://doi.org/10.1016/j.jsames.2010.02.001>
- Teixeira, L. R. (2008). Projeto Barra-Oliveira dos Brejinhos. Relatório Temático de Litogeoquímica. Brasil: Programa Recursos Minerais do Brasil.
- Teixeira, W., Sabaté, P., Barbosa, J., Noce, C. M., Carneiro, M. A. (2000). Archaean and Paleoproterozoic tectonic evolution of the São Francisco Craton. In: U. G. Cordani, E. J. Milani, A. Thomaz Filho, D. A. Campos (Eds.), Tectonic evolution of South America, v. 1, p. 107-137. *31st International Geological Congress*. Rio de Janeiro.
- Thomas, H. V., Large, R. R., Bull, S. W., Maslennikov, V., Berry, R. F., Fraser, R., Froud, S., Moye, R. (2011). Pyrite and pyrrhotite textures and composition in sediments, laminated quartz veins, and reefs at Bendigo Gold Mine, Australia: insights for ore genesis. *Economic Geology*, 106(1), 1-31. <https://doi.org/10.2113/econgeo.106.1.1>
- Varjão, L. M. P., Leal, A. B. M. (2019). Geoquímica dos diques máficos de Brumado, porção sudeste do Bloco Gavião, Bahia, Brasil. *Geologia USP Série Científica*, 19(3), 237-252. <https://doi.org/10.11606/issn.2316-9095.v19-144710>
- Vasconcelos, A. D., Gonçalves, G. O., Lana, C., Buick, I. S., Kamo, S. L., Corfu, F., Scholz, R., Alkmim, A., Queiroga, G., Nalini Jr., H. A. (2018). Characterization of xenotime from Datas (Brazil) as a potential reference material for in situ U-Pb geochronology. *Geochemistry, Geophysics, Geosystems*, 19(7), 2262-2282. <https://doi.org/10.1029/2017GC007412>
- Warr, L. N. (2021). IMA-CNMNC approved mineral symbols. *Mineralogical Magazine*, 85(3), 291-320. <https://doi.org/10.1180/mgm.2021.43>